Journal of Biomedical Materials Research Part A

WILEY

Society For Biomaterials

RESEARCH ARTICLE

In Vitro Osteogenic Response to Copper-Doped Eggshell-Derived Hydroxyapatite with Macrophage Supplements

Tejal V. Patil[1,2] | Dinesh K. Patel[3] | Ki-Taek Lim[1,2,4]

[1]Department of Biosystems Engineering, Kangwon National University, Chuncheon, Republic of Korea | [2]Interdisciplinary Program in Smart Agriculture, Kangwon National University, Chuncheon, Republic of Korea | [3]School of Chemical Engineering, Yeungnam University, Gyeongsan, Republic of Korea | [4]Institute of Forest Science, Kangwon National University, Chuncheon, Republic of Korea

Correspondence: Ki-Taek Lim (ktlim@kangwon.ac.kr)

Received: 5 June 2024 | **Revised:** 22 October 2024 | **Accepted:** 7 November 2024

Funding: This study was supported by the 'Basic Science Research Program' through the 'National Research Foundation of Korea' funded by the 'Ministry of Education' (NRF-2018R1A16A1A03025582; NRF2022R1I1A3063302). This work was supported by the Innovative Human Resource Development for Local Intellectualization program through the Institute of Information & Communications Technology Planning & Evaluation (IITP) grant funded by the Korea government (MSIT) (IITP-2024-RS-2023-00260267).

Keywords: conditioned medium and osteogenesis | cytotoxicity | hydroxyapatite | mineralization

ABSTRACT

The high bioactivity and biocompatibility of hydroxyapatite (HAP) make it a useful bone graft material for bone tissue engineering. However, the development superior osteoconductive and osteoinductive materials for bone regeneration remains a challenge. To overcome these constraints, Cu-doped hydroxyapatite (HAP(Cu)) from waste eggshells has been produced for bone tissue engineering. The materials produced were characterized using Fourier transform infrared spectroscopy, x-ray diffraction, and photoelectron spectroscopy. The scanning microscopy images revealed that the developed HAP was a rod-like crystalline structure with a typical 80–150 nm diameter. Energy-dispersive x-ray spectroscopy showed that the generated HAP was mostly composed of calcium, oxygen, and phosphorus. The Ca/P molar ratios in eggshell-derived and copper-doped HAP were 1.61 and 1.67, respectively, similar to the commercially available HAP ratio (1.67). The WST-8 assay was used to assess the biocompatibility of HAPs with hBMSCs. HAP(Cu) in the media significantly altered the cytotoxicity of biocompatible HAP(Cu). The osteogenic potential of HAP(Cu) was demonstrated by greater mineralization than that of pure HAP or the control. HAP(Cu) showed higher osteogenic gene expression than pure HAP and the control, indicating its stronger osteogenic potential. Furthermore, we assessed the effects of sample-treated macrophage-derived conditioned medium (CM) on hBMSCs' osteogenesis. CM-treated HAP(Cu) demonstrated a significantly higher osteogenic potential vis-à-vis pure HAP(Cu). These findings revealed that HAP(Cu) with CM significantly improved osteogenesis in hBMSCs and can be explored as a bone graft in bone tissue engineering.

1 | Introduction

Millions of people worldwide suffer from bone defects annually. Trauma, congenital anomalies, tissue resection due to cancer, and infection play significant roles in bone loss [1]. Autografts and allografts are frequently used for reconstructive management of large bone defects. Autografts are considered the gold standard for managing large bone defects. The limited availability, prolonged wound drainage, and repeated surgery of the donor restrict the broad applicability of the autograft process [2, 3]. In

Tejal V. Patil and Dinesh K. Patel contributed equally to this work.

contrast to autografts, allografts provide an alternative approach for managing bone defects owing to the availability of a donor site and lack of morbidity [4]. However, immunological rejection and risk of contamination can cause serious problems during the allograft process. Therefore, it is necessary to develop cost-effective approaches for rapid bone regeneration. In this regard, the tissue engineering approach is vital for restoring and maintaining tissue function using developed biological substitutes. Various biological substitutes, including calcium sulfate, bioactive glass, calcium phosphate, and polymer-based grafts, have been utilized in bone tissue engineering [4–6]. Mehnath and co-workers coated Ti-6Al-4V with minerals and marine sponges and examined its osteoinductive potential. They primarily focused on the cytotoxicity and adhesion of osteoblasts to the developed scaffolds [7]. In another study, Mehnath et al. developed bone-adhesive hydrogels for bacterial eradication and osteoblast regeneration. They highlighted the antibacterial activity of hydrogels through various interactions [8]. Xue and co-workers developed biodegradable multifunctional bioactive glass nanoparticle for photothermal-chemotherapy and bone regeneration applications. The developed materials showed excellent stimuli-responsive drug release, antibacterial potential, and bone-healing ability in rat cranial defects. However, the developed scaffolds moderately accelerated the regeneration efficiency [9]. Therefore, it is necessary to develop materials that exhibit multifunctional abilities and accelerate bone-tissue regeneration in a shorter time.

In this context, hydroxyapatite (HAP), with the general formula $Ca_{10}(PO_4)_6(OH)_2$ has received significant attention in bone tissue engineering owing to its superior biocompatibility and chemical resemblance to bone. They are widely used in implant coatings, bone substitutes, and drug delivery applications. It accelerates the new bone formation through biochemical interaction with the implant surface [10, 11]. Di-calcium phosphate dihydrate (DCPD), tri-calcium phosphate (TCP), tetra-calcium phosphate (TTCP), and octa-calcium phosphate (OCP) are used in biomedical applications [12]. Among these, HAP and TCP exhibited superior osteoconductive potential compared to the other apatites. Additionally, HAP demonstrates a wide range of pH stability (4–14) at room temperature [13]. Different methods, including chemical precipitation, sol–gel, hydrothermal, ultrasonic-chemical, solvothermal, solid-state reaction, and high-temperature treatment processes, have been explored for the synthesis of HAP. Each technique has advantages and disadvantages compared with other methods [14–16]. Chemical precursors including calcium and phosphorus have been explored for the synthesis of HAP. Waste eggshells are the most sustainable source of HAP because of their easy availability, low cost, and rich calcium content [7]. Natural bone minerals have characteristics different from those of synthetic apatites. The natural bone mineral contains different ions, such as Na^+, K^+, Sr^{2+}, F^-, and Mg^{2+}, which influence the bone activities. These ions significantly influence bone biomineralization. Pure HAP also shows inferior bioactivity compared to natural bone [17]. Ions such as Zn^{2+}, Sr^{2+}, and Mn^{2+} favor osteogenesis, whereas Mg^{2+}, Cu^+, and Co^{2+} trigger angiogenesis [10]. It is well-established that osteogenesis is limited without angiogenesis and that enhancement in vascularization is necessary for enhanced osseointegration. Thus, the development of biomaterials that show superior angiogenesis and osteogenesis potential is required for bone tissue engineering. The bioactivity and performance of synthetic apatite can be enhanced by doping with trace amounts of suitable metal ions [18]. The host cells give the immune response to foreign bodies, including biomaterials, through immune cells such as foreign body giant cells and macrophages [19]. Macrophages play a vital role in fracture healing. Monocytes accumulate in injured areas and differentiate into pro- or anti-inflammatory macrophages. These macrophages secrete different proteins and cytokines that play crucial role in tissue regeneration [20]. The surrounding microenvironment significantly and profoundly affects macrophage differentiation.

Considering the vascularization ability of copper, we developed HAP(E) from waste eggshells through ultrasonication, followed by the doping of copper into the developed HAP(E) to improve bone tissue engineering. The developed HAP was characterized through different spectroscopic techniques, including Fourier transform infrared spectroscopy, x-ray diffraction, x-ray photoelectron spectroscopy, and thermogravimetric analysis. The developed HAP exhibited a rod-like crystalline structure. The biocompatibility and osteogenic ability of the developed HAP were monitored using human bone marrow-derived mesenchymal stem cells (hBMSCs), a water-soluble tetrazolium 8 (WST-8) assay, and a real-time polymerase chain reaction. The osteogenic ability of the developed HAP was also examined in macrophage-derived conditioned media (CM). Upregulation of osteogenic gene markers was observed with Cu-doped HAP, indicating its superior osteogenic potential. To the best of our knowledge, this is the first study demonstrating the osteogenic potential of waste eggshell-derived Cu-doped HAP in macrophage-conditioned media for rapid bone tissue engineering. The antibacterial potential of the developed HAP was also monitored. A schematic representation of the development of eggshell-derived Cu-doped HAP in macrophage-conditioned media for potential bone tissue engineering is shown in Scheme 1.

2 | Experimental Section

2.1 | Materials

The waste eggshells were received from the local supplier. The ortho-phosphoric acid (H_3PO_4, 85% Duksan, Republic of Korea) and anhydrous copper sulfate ($CuSO_4$) (Alfa-Aesar, India) were used as received without further modifications. The commercially available reagent grade hydroxyapatite (HAP) was purchased from Sigma Aldrich, USA.

2.2 | Synthesis of Pure and Copper-Doped Hydroxyapatite (HAP)

Eggshell-derived HAP was synthesized as previously reported with some modifications [13]. Briefly, the waste eggshells were washed with running water to remove the impurities and inner membrane, followed by drying at 100°C for 3 days. Subsequently, the dried eggshells were heated at 300°C for 2 h to eliminate the organic content from the sample, followed by heating at 900°C for 3 h to obtain calcium oxide from the decomposition of calcium carbonate. The obtained calcium oxide was treated with the required amount of orthophosphoric acid via ultrasonication for 1 h. Cu-doped HAP was

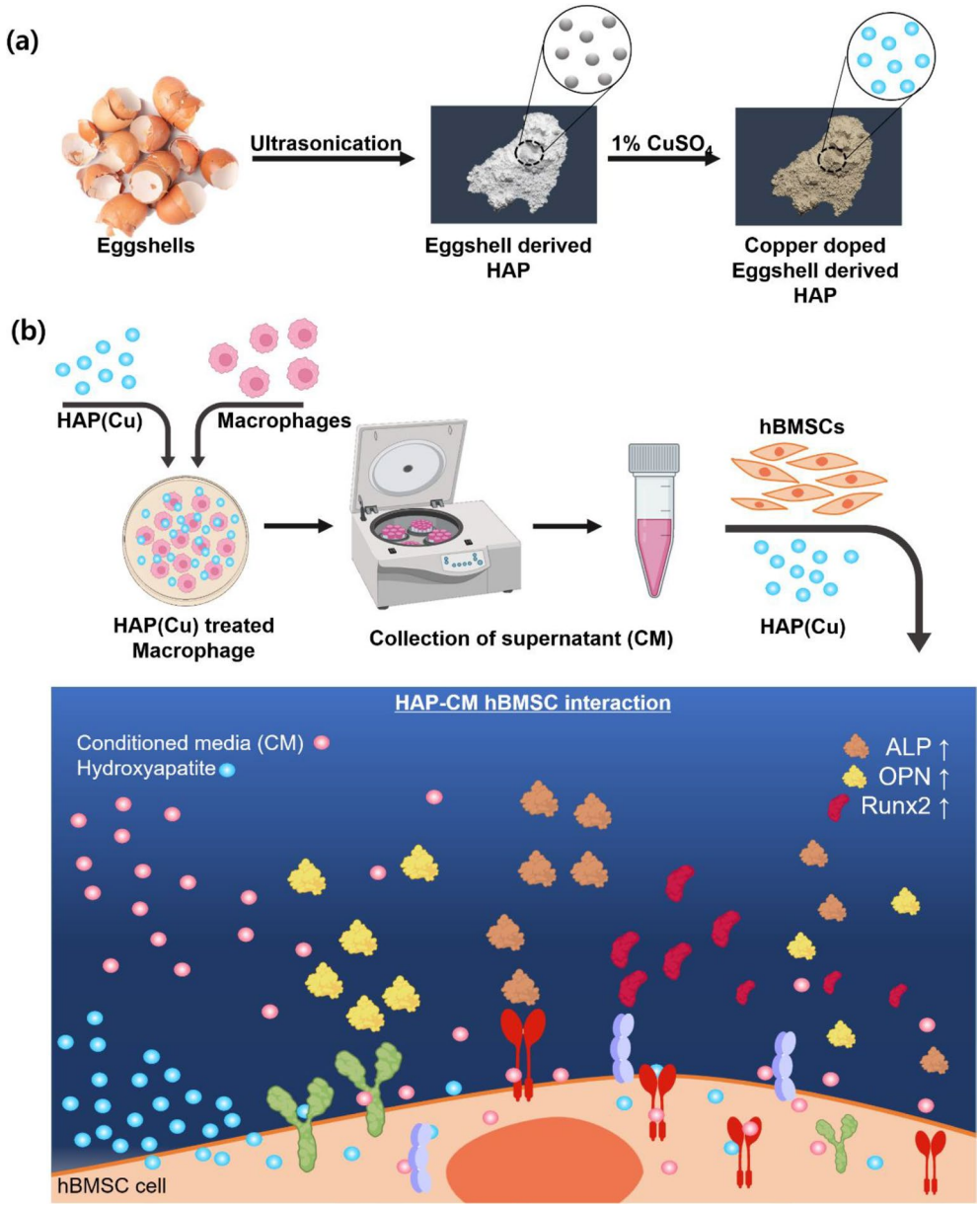

SCHEME 1 | Schematic presentation for fabricating copper doped HAP from eggshells, and their potential applications in bone tissue engineering. (a) Preparation of eggshell-derived hydroxyapatite HAP(E) and HAP(Cu) through chemical treatment, and (b) Preparation of macrophage-conditioned media with HAP(Cu) and their plausible applications in bone tissue engineering.

developed by adding 1 wt.% copper sulfate in the calcium oxide and orthophosphoric acid reaction medium, followed by ultrasonication for 1 h. The resulting material was filtered and washed with water. The obtained materials were air-dried at 80°C for 2 days. Subsequently, the materials were calcined in an oven at 900°C for 5 h to remove impurities, such as carbonates, and achieve standard HAP. The calcined samples were used in this study. The details of the processes for simulated body fluid (SBF) assessment and copper release processes are provided in the Supporting Information.

2.3 | Characterizations

Fourier transform infrared (FTIR) spectroscopy (Frontier, Perkin Elmer, UK) examined the prepared HAP's chemical composition in the 4000–500 cm^{-1} measured regions with a resolution of 4 cm^{-1}. The number of scans measured was 64. The x-ray diffractometer (XRD) (X'Pert PRO MPD, Philips, Eindhoven, Netherlands) was used to monitor the structural changes in the pure HAP and HAP(Cu) at an operating voltage and current of 40 kV and 40 mA, with Cu Kα radiation ($\lambda = 1.5414$ A°), respectively. The thermal property of the prepared HAP and HAP(Cu) was monitored by a thermal analysis system (TA Instruments, SDT Q600) in the measured regions of 40°C–600°C with a heating rate of 10°C/min in an inert atmosphere.

The morphologies of the prepared HAP and HAP(Cu) were examined by scanning electron microscopy (SEM) (S-4800, Tokyo, Japan). Elemental analysis was performed using an energy-dispersive X-ray analyzer (EDX) equipped with an

SEM instrument. The x-ray photoelectron spectrometer (XPS) (K-Alpha$^+$, Thermo Fischer, USA) was further used to examine the developed HAP and HAP(Cu) chemical compositions. The AlKα source recorded the XPS spectra at a constant pass energy of 150 eV. The C_{1s} peak was used for static sample charge correction of the recorded spectra at 284.8 eV. The copper release from HAP(Cu) was assessed using inductively coupled plasma-optical emission spectroscopy (ICP-OES, Agilent 5900).

2.4 | Cytotoxicity Examination of HAP

The cytotoxicity of the prepared HAP and HAP(Cu) was monitored using hBMSCs through the WST-8 assay at different time points (1, 3, and 5 days) and concentrations. The primary culture process for hBMSCs is described in the Supporting Information section. For this, hBMSCs (0.5×10^4 cells/well) were placed in a 96-well plate for 24 h to adhere to the plate surface. After that, the old media were changed by different concentrations (10, 30, 50, and 100 μg/mL) of sample-containing media. Groups without sample treatment were used as controls. The medium was replaced every three-day interval. After incubation, cells were washed with 1 × PBS (2 times) and 10% WST-8 dye-containing medium was added for 2 h to formazan. The developed formazan was transferred to a new plate, and absorbance was taken at 450 nm using a spectrophotometer (Infinite M Nano 200 Pro, TECAN, Switzerland). Each treatment was performed in triplicate ($n=3$). The cell viability of the control was considered 100%. The cell viability was calculated using the following equation:

$$\textit{Cell viability}\,(\%) = \frac{\textit{Optical density (OD) at 450 nm of treated group}}{\textit{Optical density (OD) at 450 nm of control}} \times 100\% \quad (1)$$

2.5 | Cell Morphology

The morphology of the sample-treated hBMSCs was visualized using an inverted fluorescence microscope (DMi8 series; Leica Microsystems, Germany) after 24 h of treatment. For this purpose, 2×10^4 cells were cultured in 24 well plates and allowed to adhere to their surfaces. The next day, the culture media was replaced by a 10 μg/mL sample containing media and incubated for 24 h. After The cells were washed with 1 × PBS (2 times) and fixed with 4% paraformaldehyde for 15 min. The cells were again washed with 1 × PBS (2 times) and permeabilized with 0.1% triton for 10 min, followed by blocking with 1% BSA solution for 45 min in dark at room temperature with continuous shaking. The blocked cells were stained with Actingreen 488 for 30 min, followed by nuclei staining with 4′,6-Diamidino-2-Phenylindole, Dihydrochloride (DAPI) for 2 min in the dark at room temperature. Excess stain was removed by washing with 1 × PBS (4 times) and adding one drop of mounting media for visualization. Images were captured using the appropriate filter channels and an inverted fluorescence microscope.

2.6 | Development of Macrophage-Conditioned Media (CM)

Macrophage-derived conditioned media (CM) were extracted using the developed HAP in the presence of Raw 246.7 cells. For this, 2×10^4 cells were placed in a 60.0 × 15.0 mm culture dish for 24 h to adhere to the surface. After that, the media was replaced with a 10 μg/mL sample containing culture media and allowed to interact with cells for 24 h. Then, the soup of the macrophage cells was collected and used for further experiments. To prepare working media, 10% conditioned media were added to the sample containing media. The experimental groups were denoted as −CM and + CM with and without conditioned media samples, respectively. Groups without sample treatment were used as controls.

2.7 | Alkaline Phosphatase (ALP) Activity

ALP activity of the prepared HAP and HAP(Cu) was assessed qualitatively and quantitatively using hBMSC cells after 7 and 14 days of incubation in osteogenic media in a 5% CO_2 incubator at 37°C. For this, hBMSC (2×10^4 cells/well) cells were placed on 24 well plates overnight, then, the old osteogenic media was changed to a sample containing osteogenic media with 10 μg/mL concentration with and without CM. The medium was changed every 3 days. After incubation, a TRACP and ALP assay kit (TAKARA, Seoul, Republic of Korea) was used, and qualitative analysis was performed using an Alkaline Phosphatase assay colorimetric kit (Abcam, Cambridge, UK). Evaluation was performed according to the manufacturer's protocol. The absorbance was recorded at 405 nm using a spectrophotometer for quantitative examination.

2.8 | Mineralization Assessment

The mineralization potential of the prepared materials was monitored using hBMSCs by the Alizarin red staining (ARS) technique after 7 and 14 days of treatment in osteogenic differentiation media as previously reported with some modifications [21]. Briefly, cells (2×10^4 cells/well) were placed in 24 well plates and allowed to adhere to the surface for 24 h. After that, the culture media was replaced with a 10 μg/mL sample containing media. The old media were replaced at 3-day intervals. After incubation, cells were rinsed with 1 × PBS (2 times), fixed with ice-cold 70% ethanol, and incubated for 15 min at room temperature. Next, the cells were washed twice with 1 × PBS, and the plate was inverted on tissue paper to remove excess PBS. Then, 1 mL ARS (40 mM, pH 4.2) was added to each well and incubated for 10 min at room temperature. Excess stain was removed by repeated washing with distilled water, and images were captured using an optical microscope (Zeiss Optical Microscope, Wurttemberg, Germany).

The formed minerals were quantified using a destaining solution containing 10% cetylpyridinium chloride and 10 nM of sodium phosphate (Sigma-Aldrich, USA). The destaining solution was

briefly added to the stained cells and incubated for 1 h. The solution was transferred to a new well plate and the absorbance was measured at 562 nm using a spectrophotometer. The mineralization potentials of the prepared HAP and HAP(Cu) were also examined with and without the CM. All experiments were performed in triplicate ($n = 3$), and the results are shown as mean OD ± SD.

2.9 | qRT-PCR Analysis

Quantitative real-time polymerase chain reaction (qRT-PCR) was performed to assess the expression of osteogenic genes, including *ALP*, osteopontin (*OPN*), and Runt-related transcription factor 2 (*RUNX2*), after 7 and 14 days of incubation with the developed materials in the presence of hBMSCs. Cells (4×10^4 cells/well) were seeded in 96-well plates and treated with a sample (10 μg/mL) containing the osteogenic medium for the desired periods. After incubation, RNA was isolated using TRIzol reagent (Invitrogen) according to the manufacturer's instructions, and cDNA was synthesized using reverse transcriptase (SuperScript IV Reverse Transcriptase, Invitrogen). The purity of RNA and cDNA was analyzed using a nanodrop of a spectrophotometer (Infinite MNano 200 Pro; TECAN, Switzerland). The qRT-PCR analysis was performed in PCR tubes using a Bio-Rad Real-Time PCR system (CFX96 Maestro Real-Time Systems, Bio-Rad, USA). The experiment was conducted in 20 μL with 2 μL of cDNA, 10 μL of SYBR green qPCR master mix, 7.6 μL of DEPC water, and 0.2 μL of each primer. Gene expression was normalized to that of glyceraldehyde-3-phosphate dehydrogenase (*GAPDH*) (housekeeping gene). The osteogenic potential of the prepared materials was also examined using CM (10%), a process similar to that described above. Each experiment was performed in triplicate ($n = 3$). The oligonucleotide primers used for qRT-PCR are listed in Table S1.

2.10 | Antibacterial Examination

The antibacterial potential of the prepared materials was evaluated using optical density and agar diffusion assays as previously described [22]. Briefly, a few colonies of *Escherichia coli* (*E. coli*) and *Staphylococcus epidermidis* (*S. epidermidis*) were suspended separately in the nutrient broth and incubated at 37°C overnight with continuous stirring (200 rpm) to gain the fresh bacteria colonies. The optical density of the newly grown bacteria optical density (OD) was measured at 600 nm using a spectrophotometer. The concentration of the cultured bacteria was adjusted to OD (600 nm) = 0.1 before starting the experiment. Samples with fixed concentration (500 μg/mL) were prepared in nutrient broth, and 100 μL of bacteria were added. The bacteria were treated with a sample for 6 h at 37°C, and OD was recorded every hour. After 6 h treatment, the culture was diluted by serial dilution till 10^{-5} dilution factor and 100 μL of bacteria were spread on nutrient agar plates. The agar plates were incubated at 37°C to grow colonies. Each experiment and each treatment in a single experiment was performed in triplicate ($n = 3$). Bacterial growth was calculated using the following equation:

$$\text{Bacterial growth rate}\,(\%) = \frac{OD(t) - OD(i)}{OD(i)} \times 100 \qquad (2)$$

where OD(t) is the OD value at various time intervals, and OD(i) is the initial OD value.

2.11 | Statistical Analysis

Statistical analyses were performed using one-way analysis of variance (ANOVA) with OriginPro 9.0 software to compare the control and treated groups and Tukey's test was performed for pair-wise comparison. All data were presented as mean ± SDs. Statistical analyses were performed to compare the control and treated groups. Statistical significance was set at $^{*}p < 0.05$ and $^{**}p < 0.01$.

3 | Results and Discussion

3.1 | Characterization of the Prepared HAP

The presence of different functional groups in the prepared materials was examined using FTIR spectroscopy. The FTIR spectra of commercially available (HAP(C)), eggshells-derived (HAP(E)), and copper-doped (HAP(Cu)) are presented in Figure 1a. The HAP(E) exhibits absorption peaks at 1090, 1020, 960, 629, 598, and 558 cm^{-1} due the different vibration modes of the phosphate groups [23]. The absorption peaks in the 900–1100 cm^{-1} region were assigned to the symmetric and asymmetric stretching of the phosphate vibration. Whereas the absorption peaks in the region 500–630 cm^{-1} are attributed to the bending vibration of P—O linkages in phosphate moieties [24]. The absorption patterns of HAP(E) resembled those of commercially available HAP(C), suggesting that this method is appropriate for developing value-added nanomaterials for the desired applications. The absorption peak (inset) at 3571 cm^{-1} in HAP(E) is assigned to the vibration mode of the O—H stretching [25]. Interestingly, the HAP(Cu) absorption pattern resembled those of HAP(E) and HAP(C), demonstrating that no structural changes occurred when Cu was inserted into the materials. Bee and co-workers also found that the insertion of silver ions had no significant effect on the structural changes, and exhibited absorption patterns similar to those of pure HAP [26].

Structural changes in the developed materials were also examined using XRD, and the diffraction patterns are shown in Figure 1b. HAP(E) exhibited sharp and similar XRD patterns to HAP(C) and previously reported materials, indicating the successful formation of crystalline and pure nanomaterials [27]. Calcination favors the generation of highly dense crystalline HAP. Our group previously reported the transformation of a less-dense and crystalline HAP derived from eggshells into a single-phase, dense, and highly crystalline HAP through heat treatment [13]. Meanwhile, HAP(Cu) exhibited additional diffraction peaks at 34.3° and 37.3° owing to the presence of the CuO moiety. This result indicated the inclusion of a Cu moiety in HAP [28]. However, no other remarkable changes in the diffraction patterns were observed for HAP(Cu), indicating that the inclusion of Cu did not introduce any new phases, and that HAP maintained a single phase. Noori and co-workers also reported similar results for 3% copper-doped HAP calcined at 850°C for 3 h. Neither copper inclusion nor calcination temperature caused

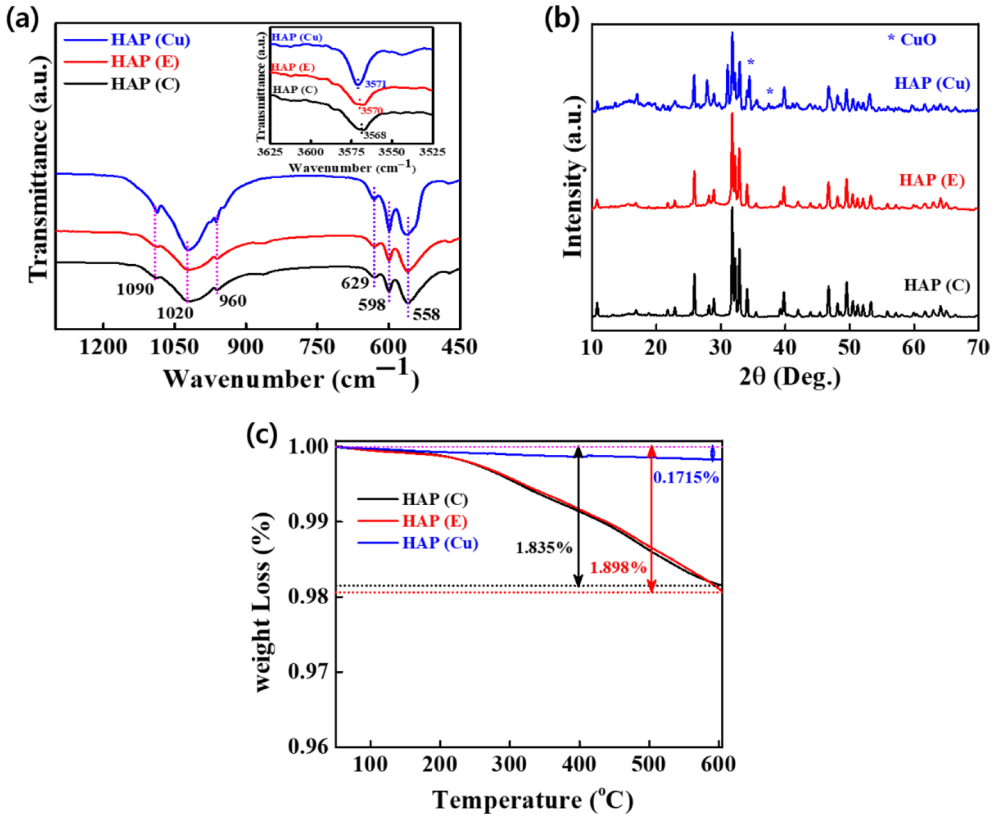

FIGURE 1 | Characterization of HAP(C), HAP(E), and HAP(Cu). (a) FT-IR spectra of the indicated HAP, (b) XRD patterns of the indicated HAP, and (c) TGA curves of the indicated HAP in the measured temperature range.

new phases in developed HAP. However, the lattice parameters increased for 1% Cu-doped HAP because of enhanced network parameters [29]. Thus, we anticipated that Cu doping would enhance the lattice parameters of the prepared materials and allow them to remain as a single phase.

The thermal stabilities of the developed materials were evaluated by thermogravimetric analysis (TGA), and the thermogram curves are presented in Figure 1c. HAP(Cu) demonstrated slightly enhanced thermal stability vis-à-vis HAP(C) and HAP(E) in the measured temperature regions. This slight enhancement in the thermal stability can be attributed to the formation of strong Cu—OH surface groups, which hindered the loss of adsorbed water. The thermal stability of a material is significantly affected by its molecular weight, degree of crystallinity, and chemical structures [30]. However, a decrease in the thermal stability has also been reported for metal (Cu, Mg, and Zn)-doped HAP, where the doped metal promoted the decomposition of HAP into TCP at higher temperatures [31]. The thermal properties provide valuable information about the lattice and coordinated water, thermal transition, material stability, and structure. In order to investigate the impact of copper incorporation into the HAP(Cu), the ions released within the medium (1×PBS), was assessed. Figure S1 illustrates a progressive escalation in the release of copper ions, suggesting a sustained release of copper ions that could potentially enhance the long term effect of HAP(Cu).

3.2 | Morphological Examination of the Prepared HAP

The morphologies of the prepared HAP were examined by FE-SEM. The images are shown in Figure 2a. The prepared HAP exhibited dense and rod-like crystalline morphology with an average length of 24.33 ± 1.5, 24.45 ± 2.1, and 53.47 ± 1.3 nm for HAP(C), HAP(E), and HAP(Cu), respectively. HAP(E) demonstrated a morphology and length nearly similar to those of HAP(C), suggesting the suitability of the applied method for converting waste materials into value-added materials. The HAP(Cu) showed a higher length compared to the HAP(C) and HAP(E), which can be attributed to the insertion of the copper moiety in the lattice. The crystal size and surface area profoundly affect cellular activity, including cell bonding and development. A larger crystal size and area favor rapid cell bonding and accelerated regeneration of new tissue [32]. The EDX spectra and elemental mapping of the prepared materials are shown in Figure 2b. The appearance of the copper diffraction peak in the EDX spectrum of HAP(Cu) further confirmed the assembly of the copper moiety in the prepared nanomaterial. The elemental mapping results of Ca, P, O, and Cu in the EDX area indicated a good distribution in the lattice. The quantitative elemental distributions of the prepared materials are presented in Table S2. The Ca/P molar ratio was 1.67, 1.60, and 1.66 for HAP(C), HAP(E), and HAP(Cu), respectively. Elemental analysis further verified the insertion of the copper moiety into HAP.

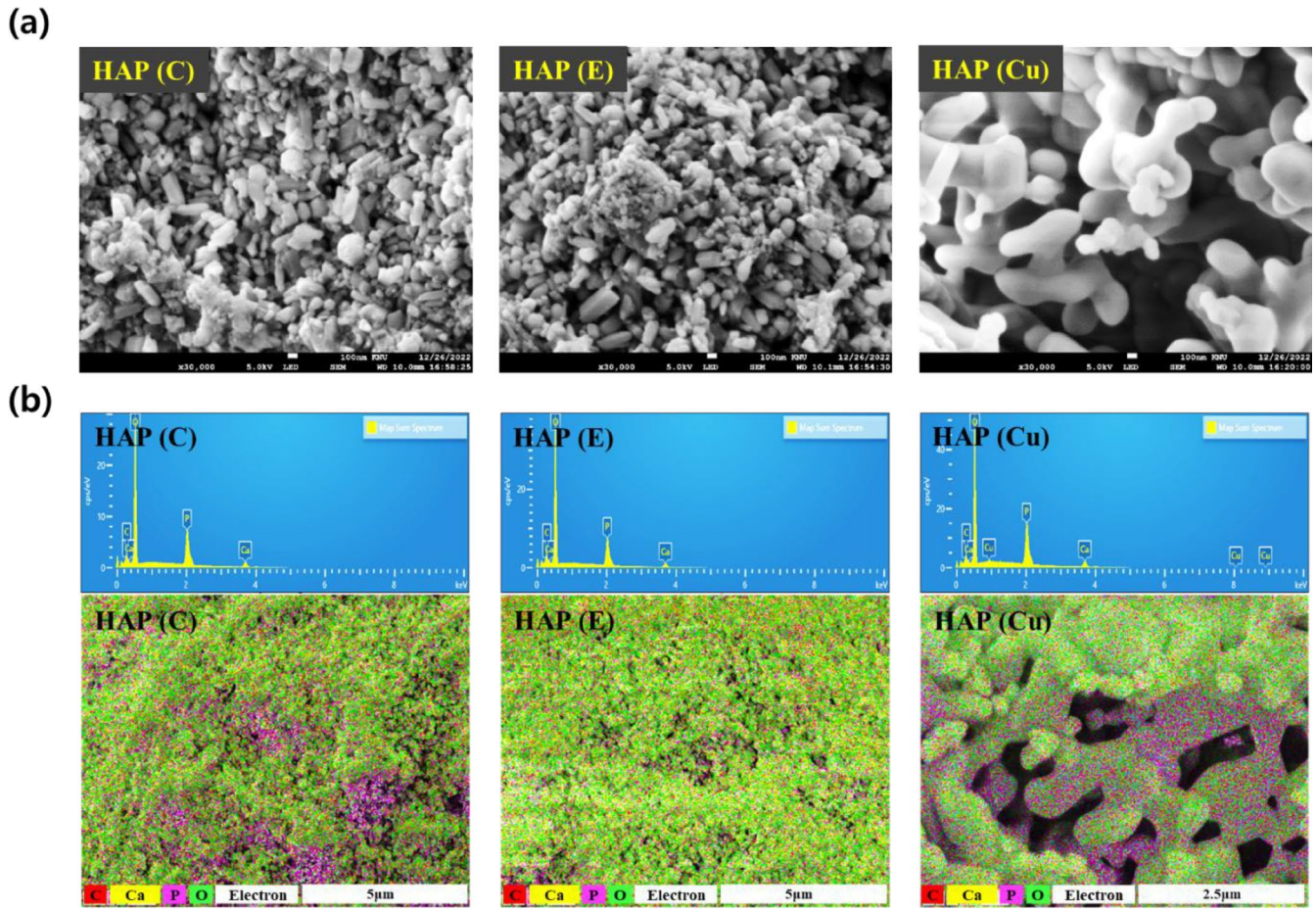

FIGURE 2 | Morphological characterization of the prepared HAP (a) FE-SEM images of the indicated HAP (scale bar: 100 nm), and (b) EDX spectra with elemental mapping of the prepared materials.

Figure S2 illustrates the surface morphology (FE-SEM) and EDS spectra of HAP(Cu) following immersion in the SBF solution for 3 and 7 days. The images reveal the presence of granular apatite crystals on the HAP(Cu) surface after 3 days of soaking. Subsequently, after 7 days of immersion, a layer of apatite crystals enveloped the HAP(Cu) particle surface. Analysis of the EDS spectra of the crystal layer on the HAP(Cu) indicated a predominant composition of calcium, phosphorus, oxygen, sodium, and magnesium.

3.3 | XPS Analysis

X-ray photoelectron spectroscopy (XPS) was performed to assess the surface characteristics of the prepared materials. The low-resolution XPS spectra of the prepared materials are shown in Figure 3a. The peaks at binding energies of 530.4, 132.3, 283.8, 346.3, and 932.3 eV are assigned to O1s, P2p, C1s, Ca2p, and Cu2p, respectively. The appearance of 932.3 eV further confirmed metal substitution in HAP [33]. The XPS spectrum of HAP(C) resembles that of HAP(E), indicating a stoichiometric relationship. The surface sites and directions significantly affected the XPS binding energies. The higher resolution spectra of O1s of the prepared HAP(E) is shown in Figure 3b. Three deconvolution peaks were observed at 530.2, 531.72, 532.62 eV for O—Ca, O—P, and O—H groups, respectively. These peaks shifted slightly towards higher binding energies in HAP(Cu), suggesting strong interactions through greater electronic delocalization [34]. The high-resolution spectra of P2p of HAP are shown in Figure 3c. A prominent peak in HAP(E) (132.29 eV) was observed due to the phosphate groups, which shifted to 133.31 eV with decreased HAP(Cu) intensity. The high-resolution spectra of C1s of the prepared materials are presented in Figure 3d. Three prominent peaks at 283.71, 284.74, and 288.02 eV were observed in HAP(E), which shifted towards higher binding energy positions in HAP(Cu). These peaks can be assigned to the surface contamination of C—H/C—C bonds, C—OH/C—O—C bonds, and C—O bonds of the adsorbed carbonate groups in the materials [26]. The high-resolution spectra of Ca2p of the materials are shown in Figure 3e. Two prominent peaks were observed in HAP(E) at 346.31 and 349.83 eV for Ca—O and Ca—P bindings, respectively. These peaks were further shifted towards higher binding energies in HAP(Cu) owing to the greater delocalization of the electronic environment. This ionic interaction of calcium ions with hydroxyl and phosphate groups resembles that of previously reported stoichiometric HAP materials, showing adequate structure and orientation of the local order in the prepared materials [35]. The high-resolution spectrum of Cu2p of the material is shown in Figure 3f. Two prominent peaks in HAP(Cu) were observed at 932.36 and 952.38 eV for $Cu2p_{3/2}$ and $Cu2p_{1/2}$ of zero-valent copper, respectively [33].

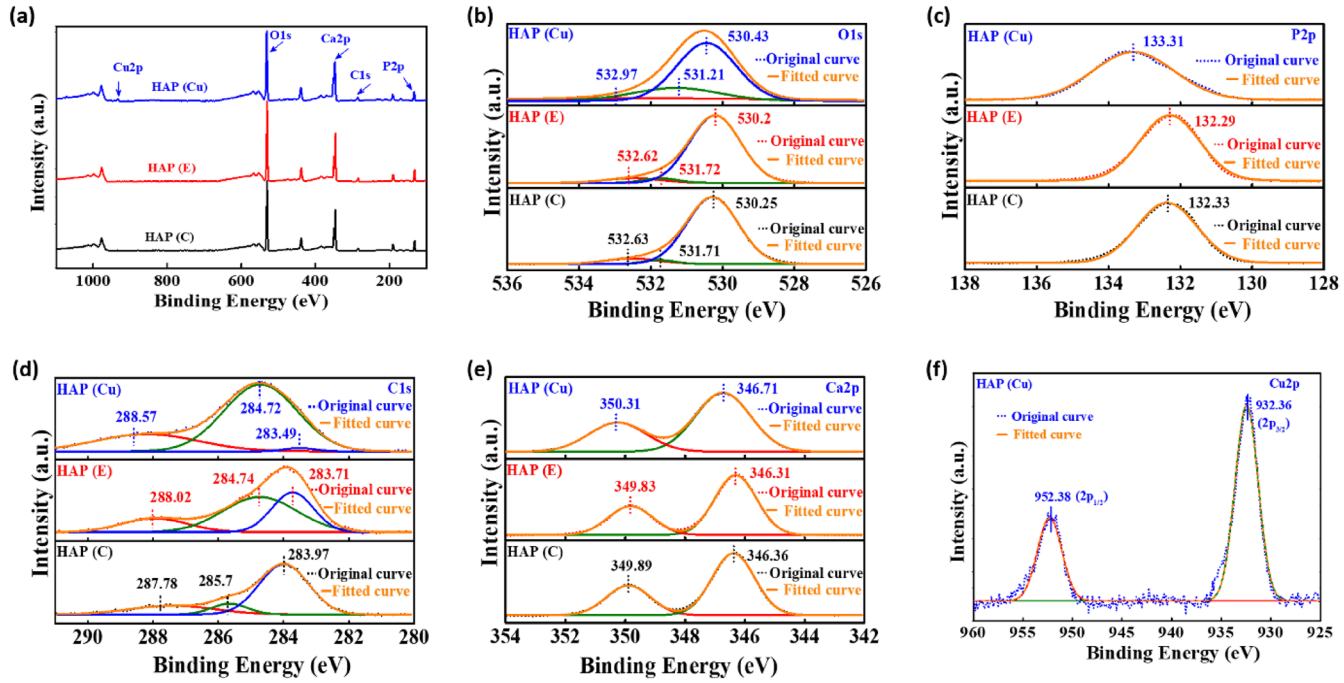

FIGURE 3 | (a) Low-resolution XPS survey spectra of HAP(C), HAP(E), and HAP(Cu), and High-resolution survey spectra for (b) O1s, (c) P2p, (d) C1s, (e) Ca2p and (d) Cu2p of HAP(Cu).

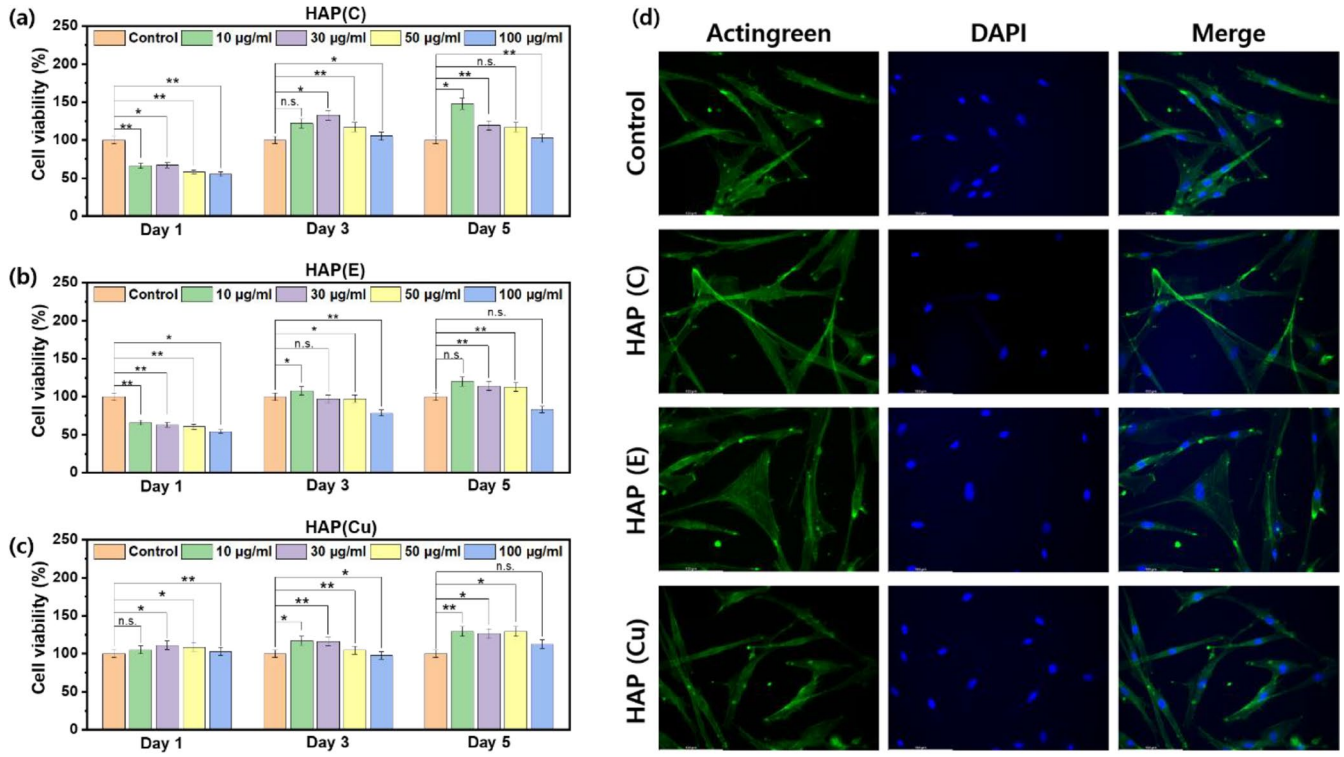

FIGURE 4 | The assessment of the cytotoxicity of the prepared materials. (a) Cell viability of hBMSC at indicated periods and concentrations with HAP(C), (b) HAP(E), (c) HAP(Cu), and (d) Fluorescence images of hBMSCs after 24 of incubation in the presence of the indicated materials at 10 μg/mL concentration. (number of replicates; $n = 4$, $^{*}p < 0.05$, and $^{**}p < 0.01$ and *n.s*: Not significant).

3.4 | Biocompatibility Assessment

The developed materials should be biocompatible with the implants and have no adverse immune responses [36]. The biocompatibility of the prepared materials was monitored with hBMSCs at different concentrations (10, 30, 50, and 100 μg/mL) for different periods (1, 3, and 5 days), and the results are presented in Figure 4. Groups without sample treatment were considered as the control group. The materials that exhibited ≥ 70% cell viability are considered biocompatible as per ISO 10993-5

classifications [37]. The viability of hBMSCs treated with different concentrations of HAP (C), HAP (E), and HAP (Cu) is shown in Figure 4a–c. HAP(C) is a well-recognized biocompatible bioceramic that is often used in implants [38]. HAP(C) and HAP(E) induced similar cell viability after 24 h of incubation at all concentrations. After 24 h of incubation, the HAP(Cu)-treated groups exhibited enhanced cell viability compared to the control and other treatments (HAP(C) and HAP(E)), indicating their superior biocompatibility. The enhanced cell viability in the HAP(Cu)-treated groups after 24 h of incubation was attributed to their rapid degradation into Ca^{2+}, P^{5+}, Cu^{2+}, OH^{-}, and oxyanions of O^{2-} which accelerate cellular activity [39]. Guo and co-workers also reported enhanced cell proliferation in copper-doped HAP-treated groups owing to the release of different ions, including Ca^{2+}, P^{5+}, and Cu^{2}, creating favorable microenvironments for improved cellular activity [40]. Cell viability further increased in all treatments with increasing incubation periods (3 and 5 days), showing good biocompatibility of the prepared materials. The amount of HAP and the incubation period profoundly affected cell viability. Among various concentrations (10, 30, 50, and 100 μg/mL), 10 μg/mL treated groups exhibited greater cell viability than others. The decrease in cell viability at higher concentrations is attributed to the formation of more reactive oxygen species, which adversely affect cellular activity and lead to a decrease in cell viability. Bazin and co-workers also reported decreased cell viability at higher concentrations of HAP due to the formation of reactive oxygen species [10]. Thus, doping eggshell-derived HAP with Cu has been proven to promote cell proliferation much more effectively than doping HAP(C) and HAP(E) at lower concentrations.

The fluorescence morphologies of the cultured cells after 1 day of treatment are shown in Figure 4d. The group without any samples was considered the control group. Here, we took 10 μg/mL concentration to visualize the effects of HAP on cell morphology due to their superior cellular activity compared to other concentrations. The cells were healthy and adhered to their surfaces. The cells exhibited elongated morphologies with higher density in HAP(Cu) than that in the other groups, indicating superior biocompatibility.

3.5 | ALP Activity

Alkaline phosphatase (ALP) plays a vital role in regulating bone mineralization. It acts as an early signal for cell differentiation in osteoblast enzymes and is essential for bone mineralization [41]. The qualitative ALP activities of HAP(C), HAP(E), and HAP(Cu) with hBMSCs after 7 and 14 days of incubation with and without CM are shown in Figure 5a. Groups without sample treatment were used as controls. The HAP-treated groups demonstrated greater ALP activity than the controls, and this was significantly higher in HAP(Cu) after 14 days of incubation, indicating superior ALP activity. The greater ALP activity of the HAP(Cu)-treated groups was attributed to their rapid decomposition into different ionic species, including Ca^{2+}, P^{5+}, Cu^{2+}, OH^{-}, and oxygen anions of O^{2-} which promoted the formation of minerals and enhanced the concentration of phosphate in the surrounding area [42]. Osteoblast membranes contain membrane-bound glycoproteins that facilitate osteogenesis by hydrolyzing pyrophosphates. Pyrophosphates prevent the formation of crystals at the calcification sites and break down organic phosphate esters, leading to higher levels of inorganic phosphates. Lin and co-workers also reported enhanced ALP activity in copper-doped calcium phosphate cement owing to the release of Cu^{2+} ions, which accelerated the deposition of minerals [43]. Furthermore, the CM-treated groups exhibited greater ALP activity than the untreated groups after 14 days of incubation. Compared to the other groups,

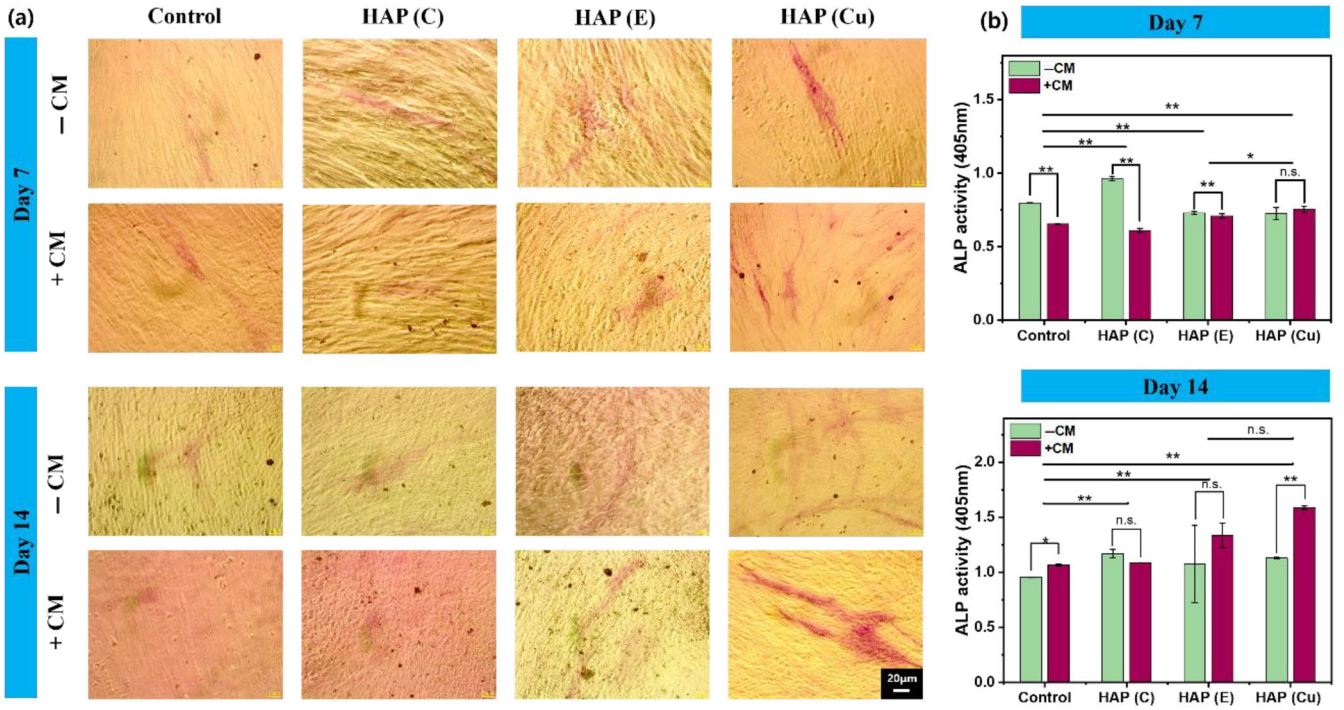

FIGURE 5 | Quantitative and qualitative analysis of ALP activity of hBMSCs in the presence of HAP samples with and without CM after 7 and 14 days. (a) ALP staining, and (b) optical density measurements. (number of replicates; $n = 3$, $^{*}p < 0.05$ and $^{**}p < 0.01$ and *n.s*: Not significant).

the enhanced ALP activity of the CM-treated groups can be attributed to the higher release of ionic species in the culture media, which promoted the formation of minerals [44]. The quantitative ALP activity of the prepared materials after 7 and 14 days of incubation with and without CM is shown in Figure 5b. Cells treated with CM showed increased ALP activity in all samples, suggesting that the amount of CM in the samples was greater than that in the pure sample groups. Increased ALP levels indicate ongoing bone remodeling. Prior research has indicated that the introduction of metal-doped hydroxyapatite triggers and enhances the process of mineralization and development of bone tissue [45]. Dopant elements can function as modulators [46]. The increased ALP activity observed with HAP(Cu) highlights its ability to promote bone formation, indicating its potential use in stimulating osteoblast development. ALP functions as a transcription factor that catalyzes the hydrolysis of phosphate esters to increase phosphate levels in specific environments. This action activates cell differentiation factors that stimulate osteoblasts [47].

3.6 | In Vitro Mineralization Efficiency of Prepared HAP

The in vitro mineralization efficiency of the materials prepared with hBMSCs was assessed using ARS after 7 and 14 days of incubation with and without CM, and the qualitative results are shown in Figure 6a. Groups without sample treatment were used as controls. Greater mineral deposition was observed in the HAP-treated groups than in the control group, indicating a superior mineralization potential. Interestingly, the HAP(Cu)-treated groups demonstrated more mineral deposition than HAP(C)-and HAP(E)-treated groups after 7 and 14 days of incubation, indicating their enhanced mineralization efficiency. The higher mineralization efficiency of HAP(Cu) can be attributed to the presence of Cu^{2+} ions in the medium, which play a significant role in mineralization and osteoblast function. Cu^{2+} ions play significant roles in angiogenesis, neuromodulation, and other metabolic activities [48]. Angiogenesis is closely associated with osteogenesis. It has been established that the Cu^{2+} ions enhanced the angiogenesis and osteogenesis by up-regulating the expression of hypoxia-inducible factor (HIF-1α) by inhibiting pyrol hydroxylases [49]. Surface texture also plays a crucial role in rapid mineralization [50]. Mehnath and co-workers reported enhanced mineralization in HAP-coated scaffolds due to their favorable surface topography, which facilitates cellular activity [51].

Furthermore, the CM-treated groups exhibited enhanced mineralization potential compared with those without CM-treated treatment after 7 and 14 days of incubation, indicating

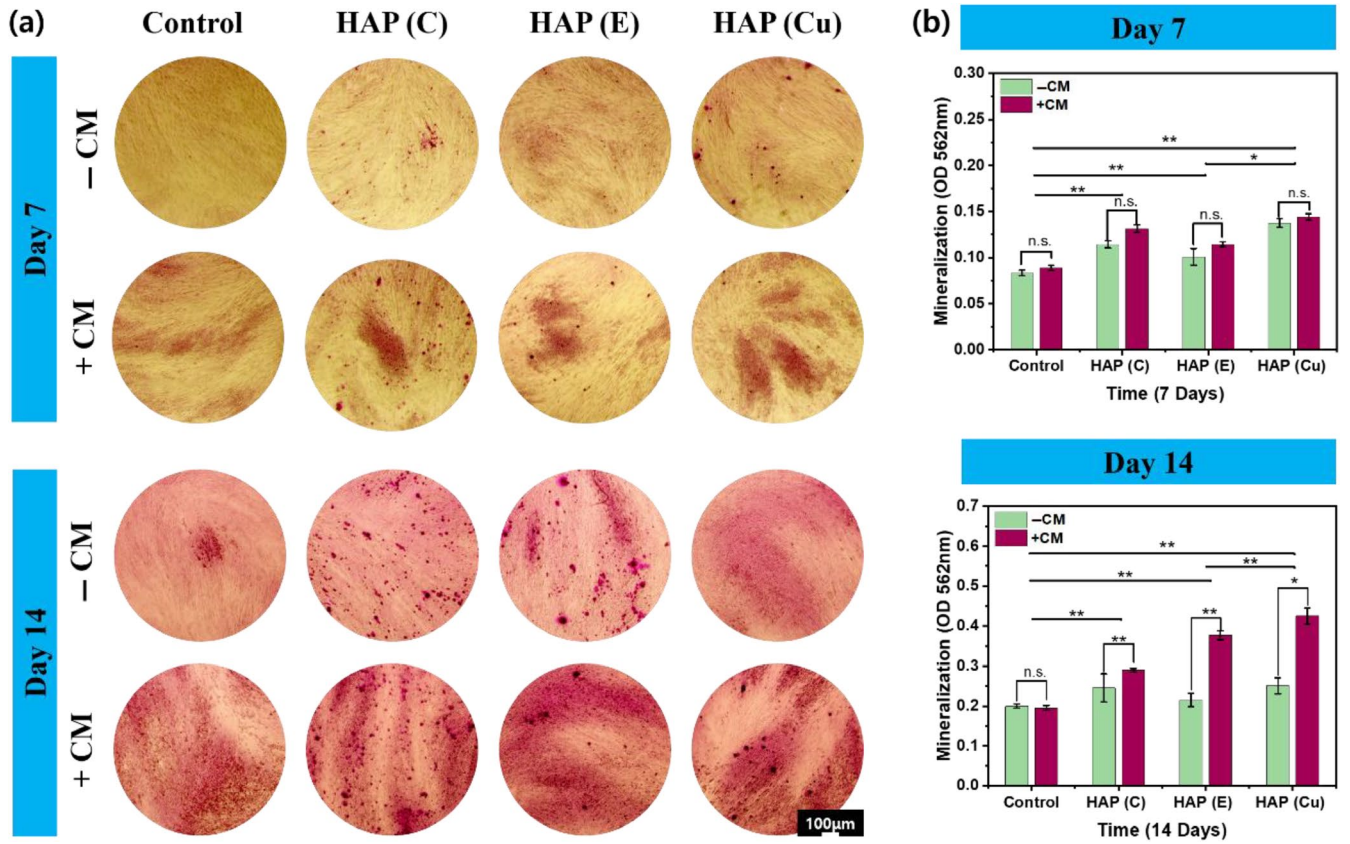

FIGURE 6 | The assessment of the osteogenic differentiation of hBMSC in the presence of the prepared HAP with and without CM at indicated periods of incubation. (a) The ARS images of hBMSC in the presence of the indicated HAP with and without CM, and (b) optical density of the destained ARS solution at indicated periods. (number of replicates; $n = 3$, $^{*}p < 0.05$, and $^{**}p < 0.01$. and *n.s*: Not significant).

the positive effects of CM on mineralization. The enhanced mineralization of the CM-treated groups was attributed to the rapid release of ionic groups in the media and the facilitation of mineral deposition. The quantitative mineralization potentials of the prepared materials with and without CM after 7 and 14 days of incubation are shown in Figure 6b. The HAP(Cu)-treated groups showed greater mineralization values than the control and others after 7 and 14 days of incubation, indicating superior mineral deposition efficiency. The high mineralization potential is due to high cellular activity, which facilitates mineralization by cell-mediated deposition of ECM constituents. The CM-treated groups demonstrated enhanced mineralization compared with the untreated group, showing positive effects on osteogenesis. Shi et al. reported the enhanced mineralization ability of Cu-doped mesoporous silica nanospheres in CM by activating the Oncostatin M (*OSM*) pathway [52].

3.7 | Osteogenic Differentiation of hBMSCs

The quantitative osteogenic potential of the prepared HAP was examined by qPCR after 7 and 14 days of incubation with and without CM, and the results are presented in Figure 7. Groups without sample treatment were used as controls. The osteogenic potential of the HAP(Cu) was assessed at 10 μg/mL due to their enhanced cellular activity at this concentration. Here, we examined the osteogenic potential of HAP(Cu) as a control because of its improved cellular activity compared to other materials. ALP is significantly expressed in mineralized tissues and is critical for hard tissue formation [47]. The CM-treated groups showed greater ALP expression than the untreated groups, indicating their potential for accelerating hard tissue formation. The HAP(Cu)-treated groups exhibited significantly enhanced ALP expression after 14 days of incubation compared to the control group, owing to their superior cellular activity. These results indicate that the developed materials have superior osteogenic potential and can be explored for use in bone tissue engineering using CM for rapid bone regeneration. The non-collagen bone matrix protein OPN is another significant osteogenic marker that controls physiological processes, such as collagen organization, cell adhesion, migration, and bone mineralization [53]. OPN expression was higher in the HAP(Cu)-treated groups than in the control group after 7 and 14 days of incubation with and without CM, indicating better osteogenic potential. OPN plays a role in maintaining the structural strength of bones and affects factors such as bone density, mineral size, and alignment. Osteoblasts synthesize OPN during the later phases of osteoblastic maturation, specifically during premineralization. OPN consists of aspartic acid residues (negatively charged motifs), which may contribute to its strong binding affinity for calcium. Thus, OPN has been proposed to regulate the formation of calcium phosphate crystals during mineralization process [54]. RUNX2 is a key regulator for osteogenesis [55]. Its expression was lower in the HAP-treated groups vis-à-vis control group after 7 days of incubation. However, it was upregulated in the HAP-treated groups after 14 days of incubation. This was further upregulated in CM-treated media, owing to better cellular activity. RUNX2, an essential osteogenic transcription factor, is a hallmark of early osteogenic differentiation. RUNX2 links multiple important signaling pathways [56]. The structural integrity of this protein makes it the master regulator of osteogenesis. RUNX2 domains interact with many proteins and regulate cellular functions through post-translational modifications in response to

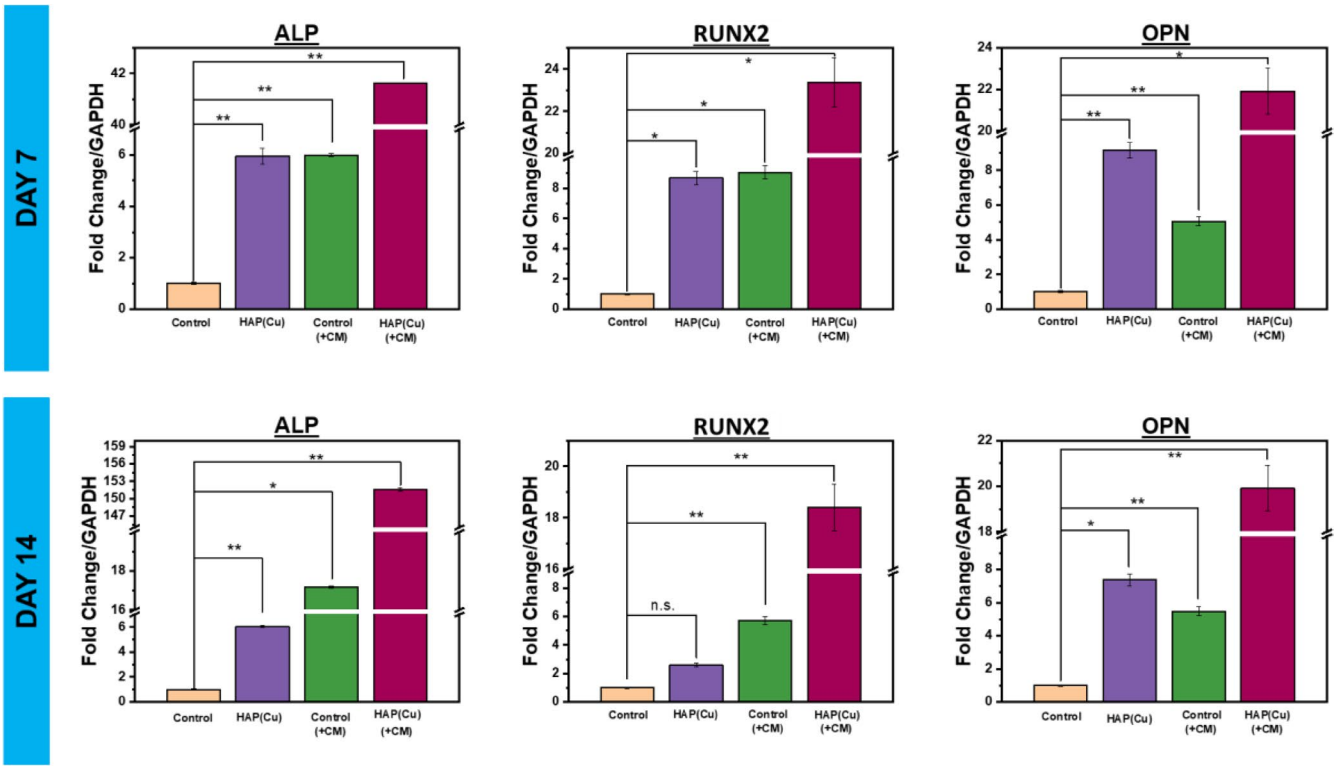

FIGURE 7 | Real-time qPCR analysis of *ALP*, *OPN*, and *RUNX2* genes after treatment of HAP(Cu) samples with and without CM for 7 and 14 days. (number of replicates; $n = 3$, $^{*}p < 0.05$ and $^{**}p < 0.01$. and *n.s*: Not significant).

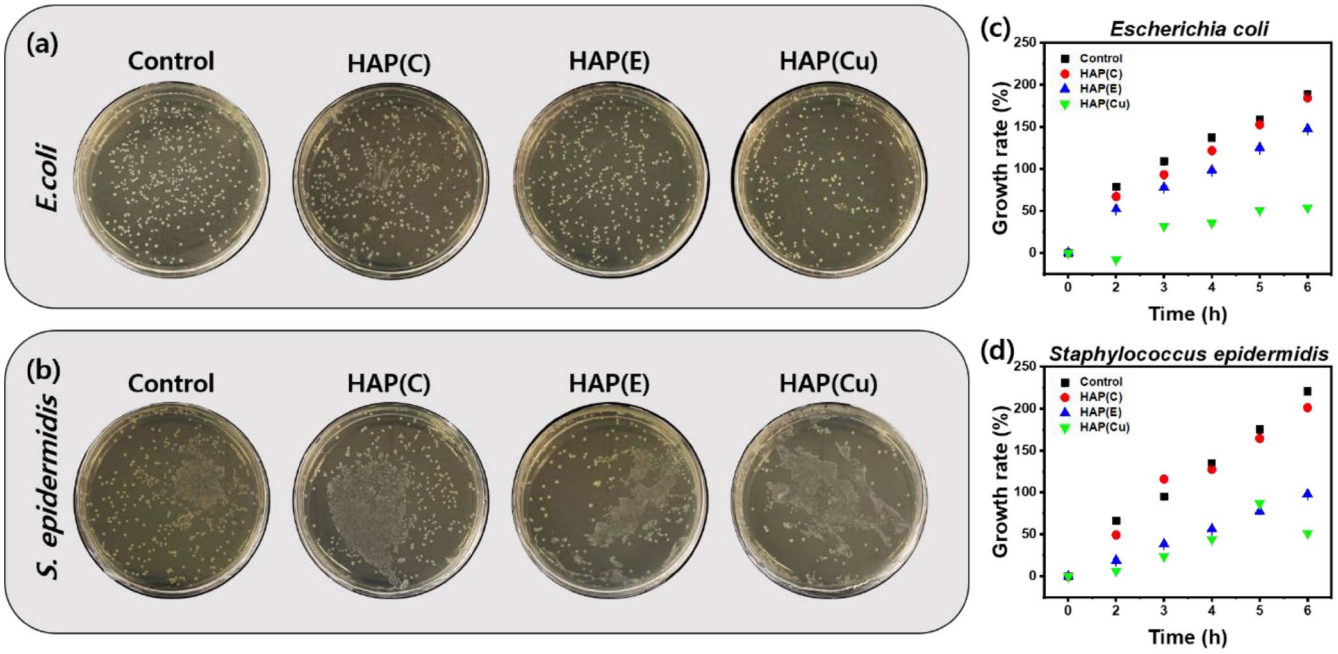

FIGURE 8 | The examination of the antibacterial potential of the prepared HAP against *E. coli* and *S. epidermidis*. (a, b) Agar plates images and (c, d) Bacteria growth rate calculated by their respective OD values at 600 nm. (number of replicates; $n = 3$).

inputs. RUNX2 is a transcription factor that differentiates and matures osteoblasts and helps create and develop bones.

3.8 | Antibacterial Activity

E. coli and *S. epidermidis* were used to monitor the antibacterial potential of the developed materials because of their susceptibility to various infections, including gastrointestinal, urinary tract, and nosocomial [57]. To effectively address the problem of bacterial infections during bone healing, which can result in surgical difficulties and necessitate the removal or replacement of implanted biomaterials, it is necessary to develop biomaterials with inherent anti-infective properties. The agar diffusion and optical density (OD) tests were conducted using HAP(C), HAP(E), and HAP(Cu) at a dose of 500 μg/mL. The bacteriostatic effectiveness of each sample was evaluated against *E. coli* and *S. epidermidis* after 6 h of incubation, and the developed colonies are shown in Figure 8a,b. Groups without sample treatment were used as controls. The HAP-treated groups exhibited fewer bacterial colonies than the control group, indicating the antibacterial potential of HAP. HAP(C) and HAP(E) exhibited minimal antibacterial activity. In contrast, fewer colonies were observed in the HAP(Cu)-treated groups, demonstrating enhanced antibacterial potential. This indicated that the incorporation of copper ions into the HAP framework enhanced its antibacterial properties.

Previous studies have shown that materials containing metal ions have two possible ways of fighting bacteria: The first involves direct bonding facilitated by electrostatic interactions, wherein metal ions (carrying a positive charge) adhere to negatively charged bacterial cell wall [58]. The second process is the impairment of the bacterial cell membrane caused by reactive oxygen species (ROS), such as superoxide (O_2^-), hydrogen peroxide (H_2O_2), and hydroxyl radical (—OH) [59]. The changes in the OD values with and without HAP after 6 h of incubation with *E. coli* and *S. epidermidis* are shown in Figure 8c,d. The control groups exhibited rapid bacterial growth compared to the HAP-treated groups. Among these (HAP(C), HAP(E), and HAP(Cu)), HAP(Cu)-treated groups demonstrated lower bacterial growth rates and superior antibacterial characteristics. Furthermore, the heightened activity level can be ascribed to various factors, including an expanded surface area that enables a more efficient release of metal ions. As previously stated, HAP(C) and HAP(E) exhibited limited antibacterial activity. Nevertheless, HAP(Cu) showed a marginal enhancement in antibacterial efficacy in this experiment, presumably because of the facilitation of contact by the inclusion of copper ions. Moreover, the cellular architecture of *E. coli* facilitates the interaction of nanoparticles with its surface. These results emphasize the potential of HAP(Cu) as a highly effective antibacterial agent with promising therapeutic results against bacterial infections. The findings of this study will facilitate the development of biomaterials with enhanced antibacterial characteristics for use in biomedical applications.

4 | Conclusion

Bone grafts have been widely used to promote bone regeneration, and their efficiency depends on their bioactivity and ability to boost osteogenic activity. HAP is considered an efficient candidate for treating bone defects due to its inherent chemical composition, which resembles the bone structure. In addition, studying this material can enhance its applicability in the development of scaffolds. This study helps to understand the osteogenic potential of waste eggshell-derived HAP and copper ion doping. The particle size and chemical composition of eggshell-derived HAP resembled the commercially available HAP. This demonstrates that wasted eggshells have a huge market for bone

implant fabrication. No significant structural changes were observed in HAP(Cu) compared to those in HAP(C) and HAP(E).

The biocompatibility and morphology of the hBMSCs treated with the samples were demonstrated. HAP(C) and HAP(E) groups exhibited initial decreases in growth on day 1. However, the percentage of viable cells increased with time, indicating that the compatibility increased. In the case of HAP(Cu), the compatibility and growth of the cells increased significantly from the initial stage. This indicates that the presence of copper ions enhances bioactivity and maintains cell interactions for cell survival. The enhanced biocompatibility of HAP(Cu) was attributed to its ability to stimulate cell adhesion, migration, and proliferation. The osteogenic efficiency of the developed materials was monitored in hBMSCs using the ARS technique, ALP activity, and the expression of osteogenic-associated gene markers. The HAP(Cu)-treated groups exhibited superior mineralization potential and upregulated osteogenic-related gene markers (*RUNX2*, *OPN*, and *ALP* activity) compared with the other treatments, indicating enhanced osteogenic efficiency. Osteogenic efficiency was further enhanced in the CM, showing positive effects on osteogenesis. These findings indicate that this method is suitable for converting waste eggshells into value-added materials for rapid bone regeneration, which can be further accelerated using CM. However, more detailed studies, including in vivo studies, are required to validate these findings for practical applications of the materials developed in the personalized healthcare sector.

Acknowledgments

This study was supported by the 'Basic Science Research Program' through the 'National Research Foundation of Korea' funded by the 'Ministry of Education' (NRF-2018R1A16A1A03025582; NRF2022R1I1A3063302). This work was supported by the Innovative Human Resource Development for Local Intellectualization program through the Institute of Information & Communications Technology Planning & Evaluation (IITP) grant funded by the Korea government (MSIT) (IITP-2024-RS-2023-00260267).

Conflicts of Interest

The authors declare no conflicts of interest.

Data Availability Statement

The data that support the findings of this study are available on request from the corresponding author. The data are not publicly available due to privacy or ethical restrictions.

References

1. F. Migliorini, G. La Padula, E. Torsiello, F. Spiezia, F. Oliva, and N. Maffulli, "Strategies for Large Bone Defect Reconstruction After Trauma, Infections or Tumor Excision: A Comprehensive Review of the Literature," *European Journal of Medical Research* 26, no. 1 (2021): 118.

2. P. Baldwin, D. J. Li, D. A. Auston, H. S. Mir, R. S. Yoon, and K. J. Koval, "Autograft, Allograft, and Bone Graft Substitutes: Clinical Evidence and Indications for Use in the Setting of Orthopaedic Trauma Surgery," *Journal of Orthopaedic Trauma* 33, no. 4 (2019): 203–213.

3. N. Yamamoto, K. Hayashi, and H. Tsuchiya, "Progress in Biological Reconstruction and Enhanced Bone Revitalization for Bone Defects," *Journal of Orthopaedic Science* 24, no. 3 (2019): 387–392.

4. N. Pajares-Chamorro and X. Chatzistavrou, "Bioactive Glass Nanoparticles for Tissue Regeneration," *ACS Omega* 5, no. 22 (2020): 12716–12726.

5. D. Ege, K. Zheng, and A. R. Boccaccini, "Borate Bioactive Glasses (BBG): Bone Regeneration, Wound Healing Applications, and Future Directions," *ACS Applied Bio Materials* 5, no. 8 (2022): 3608–3622.

6. P. Luo, L. Yu, Q. Lin, C. Wang, D. Yang, and S. Tang, "Strontium Modified Calcium Sulfate Hemihydrate Scaffold Incorporating Ginsenoside Rg1/Gelatin Microspheres for Bone Regeneration," *Frontiers in Bioengineering and Biotechnology* 8 (2020): 888.

7. E. R. Muñoz-Sanchez, C. D. Arrieta-Gonzalez, A. Quinto-Hernandez, E. Garcia-Hernandez, and J. Porcayo-Calderon, "Synthesis of Hydroxyapatite From Eggshell and Its Electrochemical Characterization as a Coating on Titanium," *International Journal of Electrochemical Science* 18, no. 9 (2023): 100204.

8. S. Mehnath, M. Sathish Kumar, K. Chitra, and M. Jeyaraj, "Bone-Adhesive Hydrogel for Effective Inhibition of M. Tuberculosis and Osteoblast Regeneration. ACS," *Infectious Diseases* 9, no. 11 (2023): 2269–2281.

9. Y. Xue, W. Niu, M. Wang, M. Chen, Y. Guo, and B. Lei, "Engineering a Biodegradable Multifunctional Antibacterial Bioactive Nanosystem for Enhancing Tumor Photothermo-Chemotherapy and Bone Regeneration," *ACS Nano* 14, no. 1 (2019): 442–453.

10. T. Bazin, A. Magnaudeix, R. Mayet, et al., "Sintering and Biocompatibility of Copper-Doped Hydroxyapatite Bioceramics," *Ceramics International* 47, no. 10 (2021): 13644–13654.

11. G. Borciani, T. Fischetti, G. Ciapetti, M. Montesissa, N. Baldini, and G. Graziani, "Marine Biological Waste as a Source of Hydroxyapatite for Bone Tissue Engineering Applications," *Ceramics International* 49, no. 2 (2023): 1572–1584.

12. H. Lu, Y. Zhou, Y. Ma, et al., "Current Application of Beta-Tricalcium Phosphate in Bone Repair and Its Mechanism to Regulate Osteogenesis," *Frontiers in Materials* 8 (2021): 698915.

13. D. K. Patel, B. Jin, S. D. Dutta, and K. T. Lim, "Osteogenic Potential of Human Mesenchymal Stem Cells on Eggshells-Derived Hydroxyapatite Nanoparticles for Tissue Engineering," *Journal of Biomedical Materials Research Part B: Applied Biomaterials* 108, no. 5 (2019): 1953–1960.

14. M. Dardouri, J. P. Borges, and A. D. Omrani, "Tailoring the Morphology of Hydroxyapatite Particles Using a Simple Solvothermal Route," *Ceramics International* 43, no. 4 (2017): 3784–3791.

15. J.-H. Jang, B. Oh, and E.-J. Lee, "Crystalline Hydroxyapatite/Graphene Oxide Complex by Low-Temperature Sol-Gel Synthesis and Its Characterization," *Ceramics International* 47, no. 19 (2021): 27677–27684.

16. H. Nosrati, R. S. Mamoory, D. Q. S. Le, C. E. Bünger, R. Z. Emameh, and F. Dabir, "Gas Injection Approach for Synthesis of Hydroxyapatite Nanorods via Hydrothermal Method," *Materials Characterization* 159 (2020): 110071.

17. R. Panneerselvam, N. Anandhan, G. Gopu, K. P. Ganesan, and T. Marimuthu, "Impact of Different Transition Metal Ions in the Structural, Mechanical, Optical, Chemico-Physical and Biological Properties of Nanohydroxyapatite," *Applied Surface Science* 506 (2020): 144802.

18. J. T. B. Ratnayake, M. Mucalo, and G. J. Dias, "Substituted Hydroxyapatites for Bone Regeneration: A Review of Current Trends," *Journal of Biomedical Materials Research Part B: Applied Biomaterials* 105, no. 5 (2017): 1285–1299.

19. E. Antmen, N. E. Vrana, and V. Hasirci, "The Role of Biomaterials and Scaffolds in Immune Responses in Regenerative Medicine: Macrophage Phenotype Modulation by Biomaterial Properties and Scaffold Architectures," *Biomaterials Science* 9, no. 24 (2021): 8090–8110.

20. Z. Liu, J. Zhu, Z. Li, H. Liu, and C. Fu, "Biomaterial Scaffolds Regulate Macrophage Activity to Accelerate Bone Regeneration," *Frontiers in Bioengineering and Biotechnology* 11 (2023): 1140393.

21. D. K. Patel, S. D. Dutta, J. Hexiu, K. Ganguly, and K.-T. Lim, "3D-Printable Chitosan/Silk Fibroin/Cellulose Nanoparticle Scaffolds for Bone Regeneration via M2 Macrophage Polarization," *Carbohydrate Polymers* 281 (2022): 119077.

22. D. K. Patel, K. Ganguly, S. D. Dutta, T. V. Patil, A. Randhawa, and K.-T. Lim, "Highly Stretchable, Adhesive, and Biocompatible Hydrogel Platforms of Tannic Acid Functionalized Spherical Nanocellulose for Strain Sensors," *International Journal of Biological Macromolecules* 229 (2023): 105–122.

23. M. Sahadat Hossain and S. Ahmed, "FTIR Spectrum Analysis to Predict the Crystalline and Amorphous Phases of Hydroxyapatite: A Comparison of Vibrational Motion to Reflection," *RSC Advances* 13, no. 21 (2023): 14625–14630.

24. R. B. Unabia, R. T. Candidato, L. Pawłowski, R. Salvatori, D. Bellucci, and V. Cannillo, "In Vitro Studies of Solution Precursor Plasma-Sprayed Copper-Doped Hydroxyapatite Coatings With Increasing Copper Content," *Journal of Biomedical Materials Research Part B: Applied Biomaterials* 108, no. 6 (2020): 2579–2589.

25. B. A. Correa-Piña, O. M. Gomez-Vazquez, S. M. Londoño-Restrepo, L. F. Zubieta-Otero, B. M. Millan-Malo, and M. E. Rodriguez-García, "Synthesis and Characterization of Nano-Hydroxyapatite Added With Magnesium Obtained by Wet Chemical Precipitation," *Progress in Natural Science: Materials International* 31, no. 4 (2021): 575–582.

26. S.-L. Bee, Y. Bustami, A. Ul-Hamid, K. Lim, and Z. A. Abdul Hamid, "Synthesis of Silver Nanoparticle-Decorated Hydroxyapatite Nanocomposite With Combined Bioactivity and Antibacterial Properties," *Journal of Materials Science: Materials in Medicine* 32, no. 9 (2021): 1–12.

27. T. Goto, S. Yin, Y. Asakura, S. H. Cho, and T. Sekino, "Simultaneous Synthesis of Hydroxyapatite Fibres and β-Tricalcium Phosphate Particles via a Water Controlled-Release Solvothermal Process," *CrystEngComm* 25, no. 14 (2023): 2021–2026.

28. K. M. Weiss, S. K. Kucko, S. Mokhtari, T. J. Keenan, and A. W. Wren, "Investigating the Structure, Solubility, and Antibacterial Properties of Silver- and Copper-Doped Hydroxyapatite," *Journal of Biomedical Materials Research Part B: Applied Biomaterials* 111, no. 2 (2022): 295–313.

29. A. Noori, M. Hoseinpour, S. Kolivand, et al., "Exploring the Various Effects of cu Doping in Hydroxyapatite Nanoparticle," *Scientific Reports* 14, no. 1 (2024): 3421.

30. M. A. Goldberg, P. V. Protsenko, V. V. Smirnov, et al., "The Enhancement of Hydroxyapatite Thermal Stability by Al Doping," *Journal of Materials Research and Technology* 9, no. 1 (2020): 76–88.

31. M. Othmani, H. Bachoua, Y. Ghandour, A. Aissa, and M. Debbabi, "Synthesis, Characterization and Catalytic Properties of Copper-Substituted Hydroxyapatite Nanocrystals," *Materials Research Bulletin* 97 (2018): 560–566.

32. G. Karunakaran, E.-B. Cho, G. S. Kumar, et al., "Mesoporous mg-Doped Hydroxyapatite Nanorods Prepared From Bio-Waste Blue Mussel Shells for Implant Applications," *Ceramics International* 46, no. 18 (2020): 28514–28527.

33. M. A. El-Aal, H. M. Ali, and S. M. Ibrahim, "Cu-Doped 1D Hydroxyapatite as a Highly Active Catalyst for the Removal of 4-Nitrophenol and Dyes From Water," *ACS Omega* 7, no. 30 (2022): 26777–26787.

34. E. O. López, P. L. Bernardo, N. R. Checca, et al., "Hydroxyapatite and Lead-Substituted Hydroxyapatite Near-Surface Structures: Novel Modelling of Photoemission Lines From X-Ray Photoelectron Spectra," *Applied Surface Science* 571 (2022): 151310.

35. J. A. Ramos Guivar, E. A. Sanches, F. Bruns, et al., "Vacancy Ordered γ-Fe2O3 Nanoparticles Functionalized With Nanohydroxyapatite: XRD, FTIR, TEM, XPS and Mössbauer Studies," *Applied Surface Science* 389 (2016): 721–734.

36. C. J. Bullock and C. Bussy, "Biocompatibility Considerations in the Design of Graphene Biomedical Materials," *Advanced Materials Interfaces* 6, no. 11 (2019): 1–15.

37. E. Jablonská, J. Kubásek, D. Vojtěch, T. Ruml, and J. Lipov, "Test Conditions Can Significantly Affect the Results of In Vitro Cytotoxicity Testing of Degradable Metallic Biomaterials," *Scientific Reports* 11, no. 1 (2021): 6628.

38. L. F. Zubieta-Otero, S. M. Londoño-Restrepo, G. Lopez-Chavez, E. Hernandez-Becerra, and M. E. Rodriguez-Garcia, "Comparative Study of Physicochemical Properties of Bio-Hydroxyapatite With Commercial Samples," *Materials Chemistry and Physics* 259 (2021): 124201.

39. A. M. Alturki, A. Abu-Rayyan, K. M. Abualnaja, D. Alhashmialameer, R. A. El-Saeed, and R. M. El-Shabasy, "Physicomechanical and Morphological Properties of Hydroxyapatite Nanocrystals Substituted With Copper–Zirconium," *Journal of Materials Research and Technology* 14 (2021): 2312–2321.

40. C. Guo, L. Li, S. Li, Y. Wang, and X. Yu, "Preparation, Characterization, Bioactivity and Degradation Behavior In Vitro of Copper-Doped Calcium Polyphosphate as a Candidate Material for Bone Tissue Engineering," *RSC Advances* 7, no. 67 (2017): 42614–42626.

41. S. Ansari, K. Ito, and S. Hofmann, "Alkaline Phosphatase Activity of Serum Affects Osteogenic Differentiation Cultures," *ACS Omega* 7, no. 15 (2022): 12724–12733.

42. J. Jeong, J. H. Kim, J. H. Shim, N. S. Hwang, and C. Y. Heo, "Bioactive Calcium Phosphate Materials and Applications in Bone Regeneration," *Biomaterials Research* 23, no. 1 (2019): 4.

43. Z. Lin, Y. Cao, J. Zou, et al., "Improved Osteogenesis and Angiogenesis of a Novel Copper Ions Doped Calcium Phosphate Cement," *Materials Science and Engineering: C* 114 (2020): 111032.

44. A. Polo-Montalvo, L. Casarrubios, M. C. Serrano, et al., "Effective Actions of Ion Release From Mesoporous Bioactive Glass and Macrophage Mediators on the Differentiation of Osteoprogenitor and Endothelial Progenitor Cells," *Pharmaceutics* 13, no. 8 (2021): 1–20.

45. X. Wang, S. Huang, and Q. Peng, "Metal Ion-Doped Hydroxyapatite-Based Materials for Bone Defect Restoration," *Bioengineering* 10, no. 12 (2023): 1–18.

46. G. Fielding and S. Bose, "SiO2 and ZnO Dopants in Three-Dimensionally Printed Tricalcium Phosphate Bone Tissue Engineering Scaffolds Enhance Osteogenesis and Angiogenesis In Vivo," *Acta Biomaterialia* 9, no. 11 (2013): 9137–9148.

47. S. Vimalraj, "Alkaline Phosphatase: Structure, Expression and Its Function in Bone Mineralization," *Gene* 754 (2020): 144855.

48. A. Jacobs, G. Renaudin, C. Forestier, J.-M. Nedelec, and S. Descamps, "Biological Properties of Copper-Doped Biomaterials for Orthopedic Applications: A Review of Antibacterial, Angiogenic and Osteogenic Aspects," *Acta Biomaterialia* 117 (2020): 21–39.

49. W. Yu, T.-W. Sun, Z. Ding, et al., "Copper-Doped Mesoporous Hydroxyapatite Microspheres Synthesized by a Microwave-Hydrothermal Method Using Creatine Phosphate as an Organic Phosphorus Source: Application in Drug Delivery and Enhanced Bone Regeneration," *Journal of Materials Chemistry B* 5, no. 5 (2017): 1039–1052.

50. S. Mehnath and M. Jeyaraj, "Antibiofilm and Enhanced Antibiotic Delivery by Halloysite Nanotubes Architected Dental Implant Against Periodontitis," *Materials Chemistry and Physics* 295 (2023): 127061.

51. S. Mehnath, V. Muthuraj, and M. Jeyaraj, "Biomimetic and Osteogenic Natural HAP Coated Three Dimensional Implant for Orthopaedic Application," *European Polymer Journal* 175 (2022): 111387.

52. M. Shi, Z. Chen, S. Farnaghi, et al., "Copper-Doped Mesoporous Silica Nanospheres, a Promising Immunomodulatory Agent for Inducing Osteogenesis," *Acta Biomaterialia* 30 (2016): 334–344.

53. B. Depalle, C. M. McGilvery, S. Nobakhti, N. Aldegaither, S. J. Shefelbine, and A. E. Porter, "Osteopontin Regulates Type I Collagen Fibril Formation in Bone Tissue," *Acta Biomaterialia* 120 (2021): 194–202.

54. M. S. Carvalho, J. M. S. Cabral, C. L. da Silva, and D. Vashishth, "Synergistic Effect of Extracellularly Supplemented Osteopontin and Osteocalcin on Stem Cell Proliferation, Osteogenic Differentiation, and Angiogenic Properties," *Journal of Cellular Biochemistry* 120, no. 4 (2018): 6555–6569.

55. C.-Y. Tang, M. Wu, D. Zhao, et al., "Runx1 Is a Central Regulator of Osteogenesis for Bone Homeostasis by Orchestrating BMP and WNT Signaling Pathways," *PLoS Genetics* 18, no. 10 (2022): e1010480.

56. S. Vimalraj, B. Arumugam, P. J. Miranda, and N. Selvamurugan, "Runx2: Structure, Function, and Phosphorylation in Osteoblast Differentiation," *International Journal of Biological Macromolecules* 78 (2015): 202–208.

57. J.-P. Gnimatin, E. W. Weyori, S. M. Agossou, and M. N. Adokiya, "Bacterial Infections Epidemiology and Factors Associated With Multidrug Resistance in the Northern Region of Ghana," *Scientific Reports* 12, no. 1 (2022): 22069.

58. M. Godoy-Gallardo, U. Eckhard, L. M. Delgado, et al., "Antibacterial Approaches in Tissue Engineering Using Metal Ions and Nanoparticles: From Mechanisms to Applications," *Bioactive Materials* 6, no. 12 (2021): 4470–4490.

59. J. Checa and J. M. Aran, "Reactive Oxygen Species: Drivers of Physiological and Pathological Processes," *Journal of Inflammation Research* 13 (2020): 1057–1073.

Supporting Information

Additional supporting information can be found online in the Supporting Information section.